

Article

# A Poly Resistor Based Time Domain CMOS Temperature Sensor with 9b SAR and Fine Delay Line

Zhiwei Xu and Sangjin Byun \* 

Division of Electronics and Electrical Engineering, Dongguk University, Seoul 04620, Korea; xzwbruce@gmail.com

\* Correspondence: sjbyun@dongguk.edu; Tel.: +82-2-2260-3331

Received: 6 March 2020; Accepted: 2 April 2020; Published: 6 April 2020



**Abstract:** This paper presents a new type of time domain CMOS temperature sensor with a 9b successive approximation register (SAR) control logic and a fine delay line. We adopted an N-type poly resistor as the sensing element for temperature linearity. The chip was implemented in a standard 0.18  $\mu\text{m}$  1P6M bulk CMOS process with general  $V_{\text{TH}}$  transistors and the active die area was 0.432  $\text{mm}^2$ . The temperature resolution was 0.49  $^{\circ}\text{C}$  and the temperature error was from  $-1.6$  to  $+0.6$   $^{\circ}\text{C}$  over the range of 0 to 100  $^{\circ}\text{C}$  after two-point calibration. The supply voltage sensitivity was 0.085  $^{\circ}\text{C}/\text{mV}$ . The conversion rate was 25kHz and the energy efficiency was 7.2 nJ/sample.

**Keywords:** temperature sensor; fine delay line; coarse delay line; SAR; time domain; CMOS integrated circuits

## 1. Introduction

Temperature sensors have been increasingly demanded in various applications such as military, aerospace, scientific research, industry, agriculture, medicine, transportation and so on. Based on the sensory device (CMOS, BJT or resistor) and the measured signal type (voltage, current, frequency, delay time, phase shift or bandwidth), they can be implemented in various ways [1–22]. In this paper, we have chosen a time domain CMOS temperature sensor by considering the following factors.

First, measuring something is to represent it by using a ratio of two quantities, i.e., one is to be measured and the other is to be a reference. For example, the height of a person can be represented by a multiple of foot length as shown in Figure 1. So, we need both the person and the reference foot length to measure the height. Even when the height is measured in a metric system, we also need both the person and the reference meter.

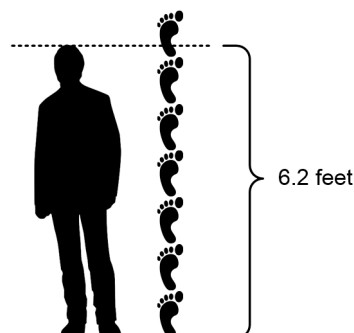


Figure 1. Measuring something is to represent it by a ratio of two quantities.

Second, measuring temperature by using a temperature sensor does not mean that we can directly measure temperature itself. What we can really measure by using a temperature sensor are the voltage or current signals or the frequencies or delay times which are one-to-one matched to the temperature.

Third, as CMOS process technology improves, the supply voltage is getting lower and lower and the clock speed is getting higher and higher, which means that the voltage resolution is degraded, whereas the time resolution is improved. This trend has naturally made time domain signal-based circuits more attractive than ever before.

Thus, in this paper we present a new type of time domain CMOS temperature sensor which can estimate temperature by measuring a frequency and a delay time. As summarized in Figure 2, a time domain temperature sensor can be implemented by choosing one among 12 types of operational principles. These operational principles have been categorized as shown in the figure based on the temperature estimation function,  $X(T)$ , which is, in this paper, defined as the ratio of two quantities chosen from  $\tau_{REF}$ ,  $\tau(T)$ ,  $1/f_{REF}$  and  $1/f(T)$ . Here,  $T$  is the temperature and  $\tau_{REF}$  is defined as a temperature-independent reference delay time of a delay cell or a delay line, and  $\tau(T)$  is defined as a temperature-dependent delay time of a delay cell or a delay line. Similarly,  $f_{REF}$  is defined as a temperature-independent reference frequency of an oscillator or a clock signal, and  $f(T)$  is defined as a temperature-dependent frequency of an oscillator or a clock signal. If we arbitrarily choose two quantities from these four different kinds of time domain signals and put them into the numerator and denominator of  $X(T)$ , respectively, overall 16 types of operational principles can theoretically exist, as shown in Figure 2. However, if the two quantities are irrelevant to  $T$  at the same time, we cannot use them for temperature estimation.

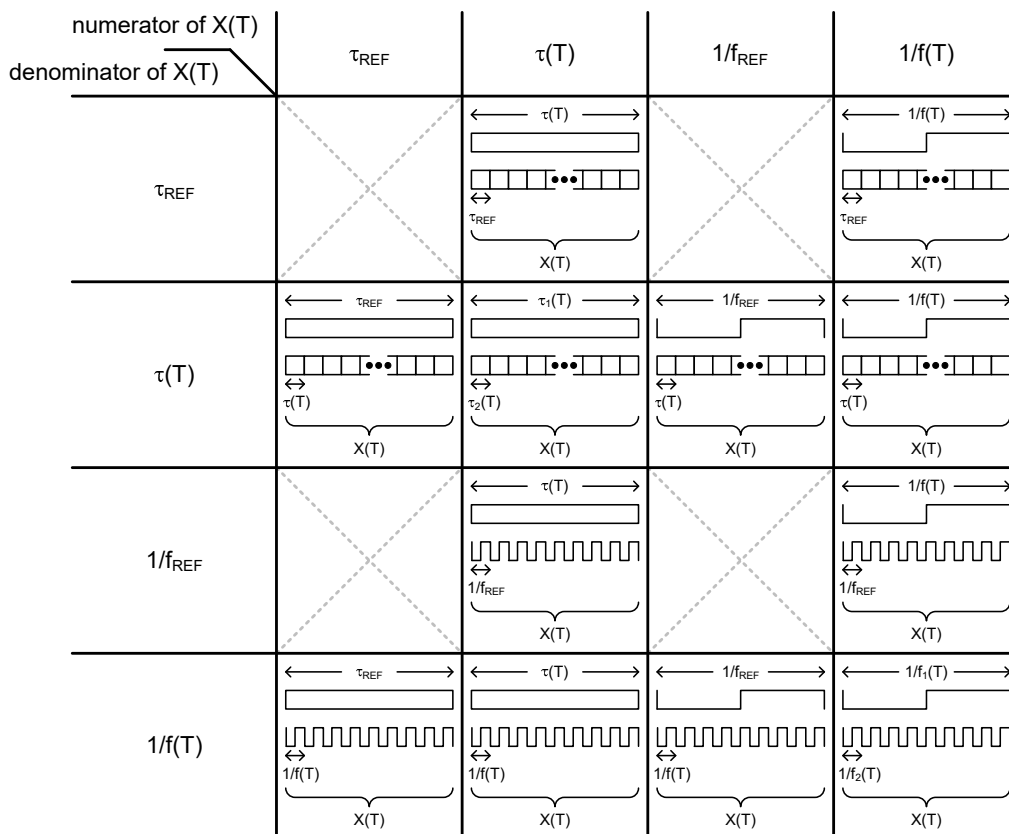


Figure 2. Twelve types of operational principles based on  $X(T)$ .

Accordingly, from the perspective of  $X(T)$ , we can newly categorize the previous time domain CMOS temperature sensors, as shown in Figure 3. In [11],  $X(T)$  is defined as the temperature-dependent delay time,  $\tau(T)$ , of an open-loop delay line divided by the reference delay time,  $\tau_{REF}$ , of a delay cell in

the reference delay locked loop (DLL). A finite state machine (FSM) is used to find out the quantized digital data which corresponds to  $X(T)$ . In [12],  $X(T)$  is defined as the temperature-dependent delay time difference,  $\tau_1(T) - \tau_{REF}$ , of two delay lines divided by the other temperature-dependent delay time,  $\tau_2(T)$ , generated from the cyclic time-to-digital converter (TDC). In [13], the temperature-dependent delay time,  $\tau_1(T)$ , of the first delay line is divided by the other temperature-dependent delay time,  $\tau_2(T)$ , of the fine delay cells in the second adjustable curvature-compensating reference delay line. A successive approximation register (SAR) control logic is used to obtain the quantized digital value of  $X(T)$ . In [14], the temperature-dependent delay time difference,  $\tau_1(T) - \tau_2(T)$ , of two delay lines is divided by the reference clock period,  $1/f_{REF}$ , of an external reference clock. In [15,16], the reference clock period,  $1/f_{REF}$ , of the temperature-independent oscillator is divided by the clock period,  $1/f(T)$ , of the temperature-dependent oscillator. In [17], the reference clock period,  $1/f_{REF}$ , of an external reference clock is divided by the clock period,  $1/f(T)$ , of the temperature-dependent oscillator. In [18], the reference clock period,  $1/f_{REF}$ , of an external reference clock is first divided by the clock period,  $1/f_1(T)$ , of the temperature-dependent oscillator and then divided by the other clock period,  $1/f_2(T)$ , of the linearity controlling oscillator, respectively. Then,  $X(T)$  is obtained by taking the difference between them, i.e.,  $X(T) = 1/f_{REF}/1/f_1(T) - 1/f_{REF}/1/f_2(T)$ . In [19,20],  $X(T)$  is defined as the first clock period,  $1/f_1(T)$ , of the temperature-dependent oscillator divided by the second clock period,  $1/f_2(T)$ , of the other temperature-dependent oscillator.

	numerator of $X(T)$			
denominator of $X(T)$	$\tau_{REF}$	$\tau(T)$	$1/f_{REF}$	$1/f(T)$
$\tau_{REF}$		[11]		
$\tau(T)$		[12], [13]	this work	
$1/f_{REF}$		[14]		
$1/f(T)$			[15] ~ [18]	[19], [20]

Figure 3. Prior works in time domain CMOS temperature sensors [11–20] and this work.

In addition to the aforementioned works shown in Figure 3, we can also design a different type of time domain CMOS temperature sensor based on the other operational principle. In this paper, we present a new type of time domain CMOS temperature sensor based on  $X(T)$  which is defined as  $X(T) = 1/f_{REF}/\tau(T)$ , as shown in Figure 3. By choosing  $X(T) = 1/f_{REF}/\tau(T)$ , we can obtain a relatively fast temperature conversion rate since the temperature sensor has  $\tau(T)$  in the denominator of  $X(T)$  and does not need to count large numbers as do the other kinds of temperature sensors, which have  $1/f(T)$  or  $1/f_{REF}$  in the denominator of  $X(T)$ . Compared to [11–13], this temperature sensor also does not need dual delay lines, since it has  $\tau(T)$  only in the denominator of  $X(T)$ .

This paper is organized as follows. In Section 2, we present the architecture and the operational principle of the implemented time domain CMOS temperature sensor. We also discuss some major aspects closely related to the performance of the temperature sensor. Section 3 explains the circuits of the main building blocks and Section 4 shows the measured results and compares the performance with the previous works. The conclusion is given in Section 5.

## 2. Architecture

Figure 4 shows the architecture of the proposed time domain CMOS temperature sensor. This temperature sensor consists of a temperature-dependent current bias circuit, a coarse delay line, a fine delay line including  $2^9$  fine delay cells, a  $2^9:1$  MUX, a 9b SAR control logic and two DFFs.

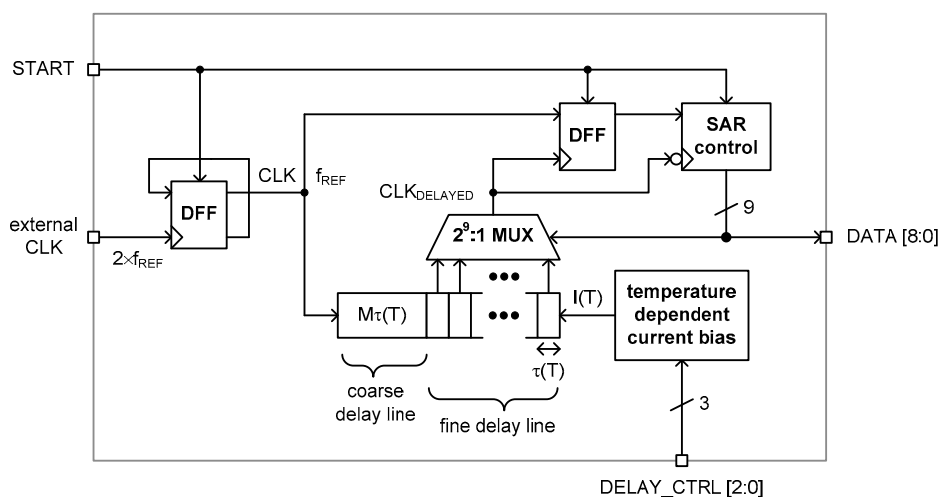


Figure 4. Architecture.

The temperature-dependent current bias circuit generates a reference current,  $I(T)$ , which is linear with the temperature. This current is fed to the coarse and fine delay lines to control the delay time of the delay lines. The delay time of the coarse delay line is designed to be about 80% of the reference clock period,  $1/f_{REF}$ , and the delay time of the fine delay line varies from 0% to about 40% of  $1/f_{REF}$  depending on the number of fine delay cells selected by the  $2^9:1$  MUX. By selecting one from  $2^9$  delayed clock signals, the DFF can compare both the rising edges of the original clock signal,  $CLK$ , and the delayed clock signal,  $CLK_{DELAYED}$ , and determine which one between  $CLK$  and  $CLK_{DELAYED}$  is faster than the other. Thus, the SAR control logic can update the 9b data,  $DATA [8 : 0]$ , repeatedly until the total delay time of the coarse and fine delay lines equals the reference clock period,  $1/f_{REF}$ . After a complete sequence of SAR operations,  $M\tau(T) + X(T)\tau(T) = 1/f_{REF}$  where  $\tau(T)$  is the delay time of the fine delay cell,  $M\tau(T)$  is the delay time of the coarse delay line and  $X(T)\tau(T)$  is the delay time of the fine delay line. This takes nine clock periods in total, i.e.,  $9/f_{REF}$ , for the SAR control logic to finish a complete sequence of SAR operations. Since the 9b output data,  $DATA[8 : 0]$ , is equivalent to the quantized digital value of  $X(T)$ ,  $X(T)$  can be represented as (1). This temperature sensor is activated by the rising edge of the external trigger signal,  $START$ .

$$X(T) = \frac{1}{\tau(T)} - M \quad (1)$$

Meanwhile, the performances of this temperature sensor were closely related to the following factors: temperature linearity, process variation compensation and supply voltage insensitivity.

Having a good temperature linearity means that  $X(T)$  can be approximately expressed as  $X(T) = aT + b$ , where  $a$  and  $b$  are constants. If  $X(T)$  is linear with  $T$ , then we can accurately estimate temperature by simply measuring  $X(T)$  and by using linear interpolation. Thus, selecting the most appropriate one from various sensing elements available in the standard CMOS processes such as mobility, threshold voltage, resistance and so on, is important for good temperature linearity. Among them, mobility has relatively poor temperature linearity and threshold voltage is not easy to manipulate [11–14]. Since poly resistors have relatively good temperature linearity and are easy to manipulate, we simulated the temperature linearity of n-type and p-type poly resistors as summarized in Figure 5. In this figure,  $R_N(T)$  and  $R_P(T)$  are the resistances of n-type and p-type poly resistors, respectively. Here,

the temperature-dependent variation was normalized with respect to the value measured at 25 °C and the linearity error was defined as the deviation (%) from the linear fit of the values of  $R(T)$  or  $1/R(T)$  over the range of 0 to 100 °C. As a sensing element, we chose  $1/R_N(T)$  in this work because  $R_P(T)$  and  $1/R_P(T)$  were useless because they were almost constant over the range of 0 to 100 °C as shown in Figure 5c,d. Between  $1/R_N(T)$  and  $R_N(T)$ ,  $1/R_N(T)$  had better temperature linearity than  $R_N(T)$ , as shown in Figure 5a,b. Over the range of 0 °C to 100 °C,  $1/R_N(T)$  changed by up to 16% and had the low linearity error of  $\pm 0.12\%$ , as shown in Figure 5b.

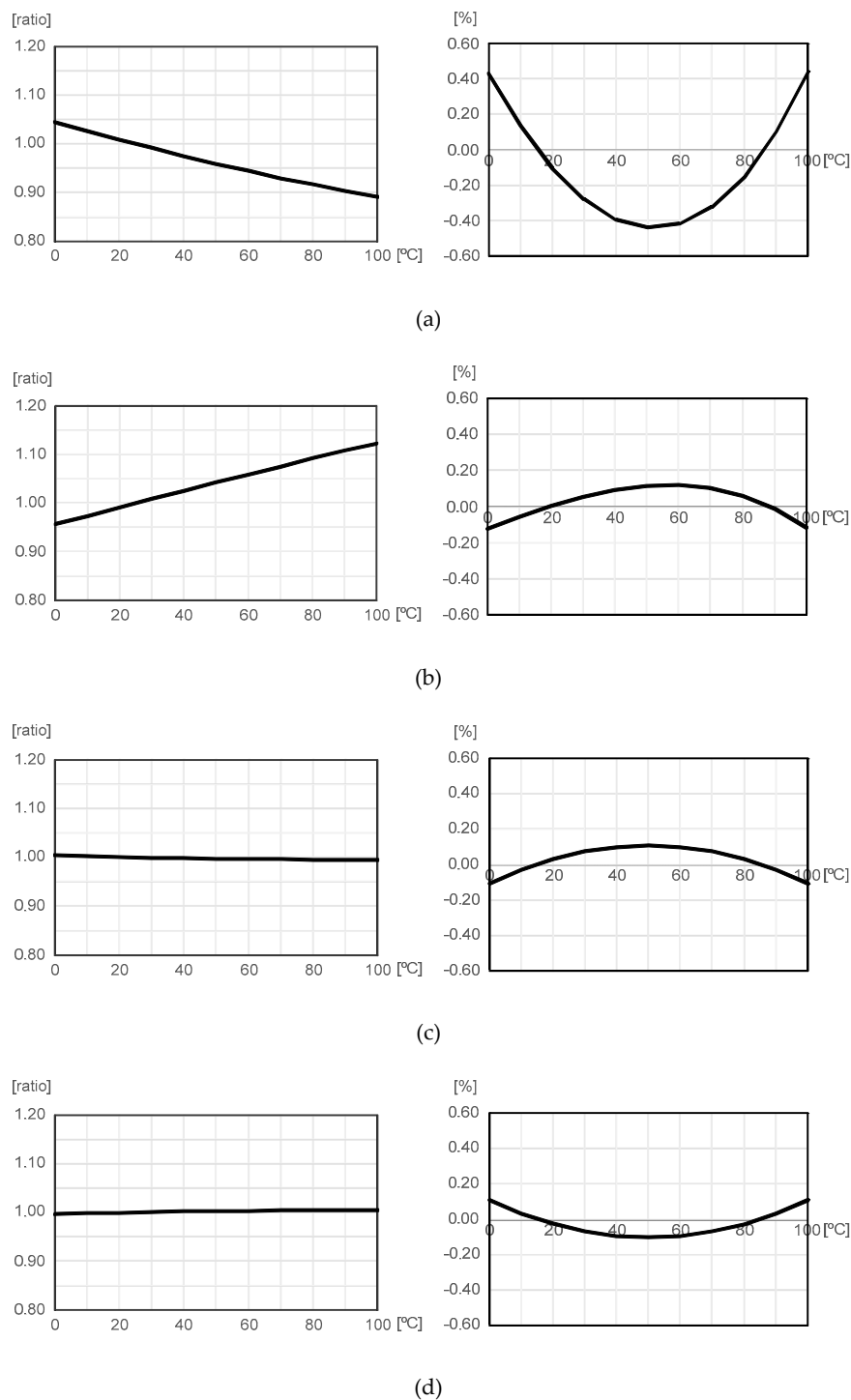


**Figure 5.** Temperature-dependent variation and linearity error of (a)  $R_N(T)$ , (b)  $1/R_N(T)$ , (c)  $R_P(T)$  and (d)  $1/R_P(T)$ .

Since the process corner is determined during chip fabrication, the chip characteristic is time-invariant after chip-out. That is, once we know the values of  $a$  and  $b$  in  $X(T) = aT + b$ , we can use them repeatedly for temperature estimation thereafter. Thus, we needed to carry out two-point calibration to find out the values of  $a$  and  $b$ . Specially, only if  $X(T) = aT$ , or in other words,  $b = 0$ , one-point calibration may be used for process variation compensation.

The values of  $a$  and  $b$  are actually affected if the supply voltage is shifted from its nominal value. To suppress the supply voltage sensitivity, we can choose one of the following options. The first option is to use an additional regulator for the temperature sensor [2,17,21]. The second option is to carefully devise a supply voltage-insensitive architecture such that the values of  $a$  and  $b$  are independent of the supply voltage variation. For this purpose, we can make the numerator and the denominator of  $X(T)$  equally affected by the supply voltage variation or not affected by the supply voltage variation at all. In this paper, we tried to make the numerator and the denominator of  $X(T)$  be as little affected by the supply voltage variation as possible.

### 3. Circuit Implementation

#### 3.1. Temperature-Dependent Current Bias Circuit

Figure 6 is the temperature-dependent current bias circuit implemented in a standard 0.18  $\mu\text{m}$  1P6M bulk CMOS technology with general  $V_{\text{TH}}$  transistors. This circuit generates a reference current,  $I(T)$ , which is inversely proportional to the resistance of an n-type poly resistor,  $R_N(T)$ . By placing three diode-connected PMOS transistors in series between  $V_{\text{DD}}$  and  $0\text{V}$ , we can obtain the reference voltage,  $V_{\text{REF}}$ , which equals  $2 \times V_{\text{DD}}/3$ . Since  $M_{\text{P1}}$  and  $M_{\text{P2}}$  are matched, the current-mirrored reference current can be expressed as follows:

$$I(T) = \frac{V_{\text{REF}}}{R_N(T)} = \frac{\frac{2}{3}V_{\text{DD}}}{R_N(T)} \quad (2)$$

Figure 7 shows the n-type poly resistor of the temperature-dependent current bias circuit. It can be tuned by the external 3b digital control word,  $\text{DELAY\_CTRL}[2:0]$ . We implemented this digitally tunable n-type poly resistor array to roughly compensate for the probable severe process variation of the n-type poly resistor. If the resistance is shifted too far from its nominal value in the worst case corner, we cannot expect constant power consumption for this temperature sensor. Thus, the rough resistance tuning process should be carried out before two-point calibration.

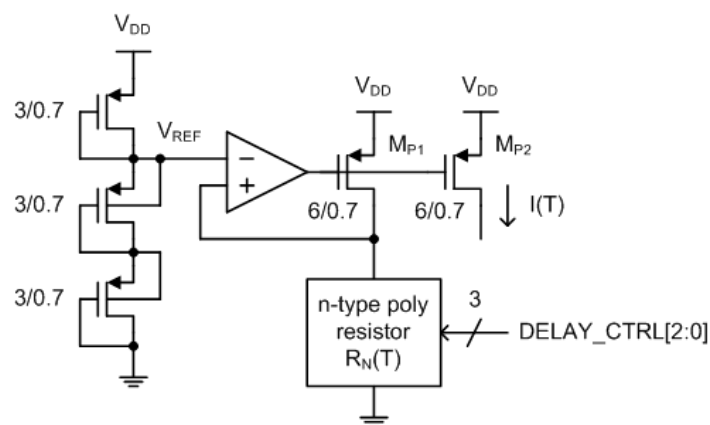


Figure 6. Temperature-dependent current bias circuit.

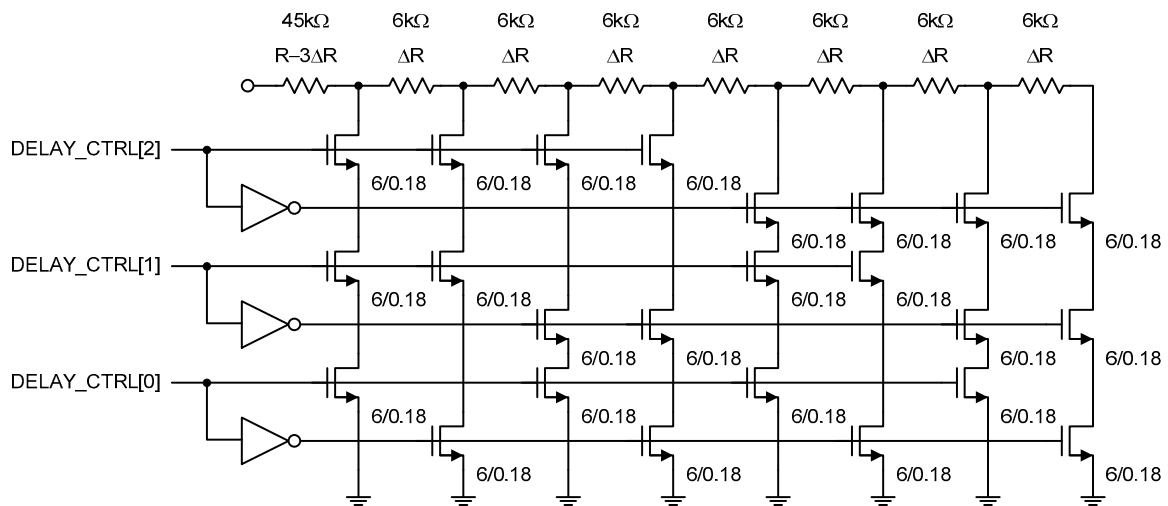


Figure 7. Digitally tuned n-type poly resistor.

### 3.2. Fine Delay Cell

Figure 8 shows the schematic of the fine delay cell. It is composed of a current-starved inverter followed by a PMOS capacitor and a normal inverter. The current-starved inverter has only a PMOS current source, such that the low to high propagation delay time of the delayed clock signal at node X was determined by the reference current,  $I(T)$ , and the total capacitance,  $C$ , seen at node X. Contrarily, the high to low propagation delay time is very small and not affected by  $I(T)$  at all. The total capacitance,  $C$ , at node X is the sum of all kinds of parasitic capacitances of  $M_1 \sim M_6$ , in addition to the MOS gate capacitance of  $M_4$ .

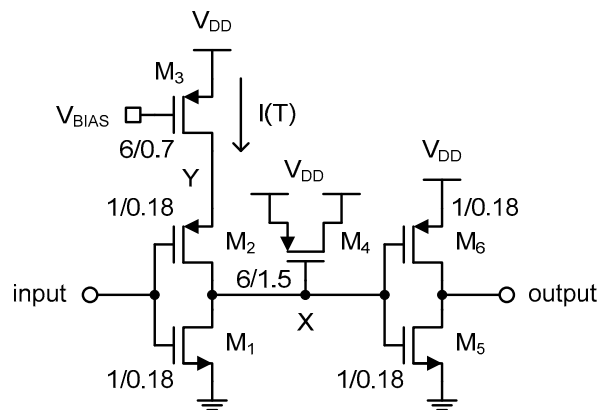


Figure 8. Fine delay cell.

Figure 9 shows the simulated and theoretical waveforms of the input and output clock signals of the fine delay cell. The delayed clock signal at node X is also denoted in red. As shown in the figure, the delayed clock signal at node X goes through three different slope regions when rising up from 0V to  $V_{DD}$ . The first slope is related to the charge sharing between node X and node Y of Figure 8 right after  $M_2$  is turned on. When the input clock signal is initially high, as shown in Figure 9b,  $M_2$  and  $M_3$  are both turned off, and so the voltage at node Y is charged to  $V_{DD}$ . When  $M_2$  is turned on by the falling edge of the input clock signal, the charge stored at node Y is instantly shared with node X right before  $I(T)$  of  $M_3$  starts charging the total capacitance,  $C$ , at node X. Thus, the second slope is determined by  $I(T)$  and  $C$ . The delay time,  $\tau_0(T)$ , in this region can be expressed as

$$\tau_0(T) = \left( \frac{V_{DD}}{2} - V_{CS} \right) \times \frac{C}{I(T)} \quad (3)$$

where  $V_{CS}$  is the charge-shared voltage and  $\tau_{CS}$  is the short delay time during charge sharing. Finally, the third slope differs from the second slope and shows up when  $V_{SG}$  of  $M_4$  decreases to be smaller than the threshold voltage of  $M_4$ , and so the PMOS gate oxide capacitance is abruptly reduced, as shown in Figure 10. Since the total capacitance,  $C$ , at node  $X$  is reduced while  $I(T)$  is kept constant, the slope steepens correspondingly. To prevent the low to high propagation delay time of the delayed clock signal at node  $X$  from being affected by this third slope region, we used the PMOS capacitor rather than the NMOS capacitor, as shown in Figure 8. Additionally,  $\tau_{PHL}$  is the high to low propagation delay time of the output clock signal. Thus, the delay time,  $\tau(T)$ , of the fine delay cell can be represented as

$$\tau(T) = \tau_{CS} + \tau_0(T) + \tau_{PHL} = \tau_{CS} + \left(\frac{V_{DD}}{2} - V_{CS}\right) \times \frac{C}{I(T)} + \tau_{PHL} \tag{4}$$

For simplicity of analysis, we assume that  $\tau_{CS}$  and  $\tau_{PHL}$  are much smaller than  $\tau_0(T)$ , and  $V_{CS}$  is also much smaller than  $V_{DD}$ , respectively. Then, the delay time of the fine delay cell can be approximately represented as

$$\tau(T) \approx \frac{V_{DD}C}{2I(T)}. \tag{5}$$

Now, by substituting (2) and (5) into (1), we can obtain the  $X(T)$  of this temperature sensor as follows:

$$X(T) = \frac{4}{3f_{REF}R_N(T)C} - M \tag{6}$$

In Section 2, we chose  $1/R_N(T)$  as the sensing element of this temperature sensor. Now we can see that  $X(T)$  is linear with  $1/R_N(T)$  as expected.

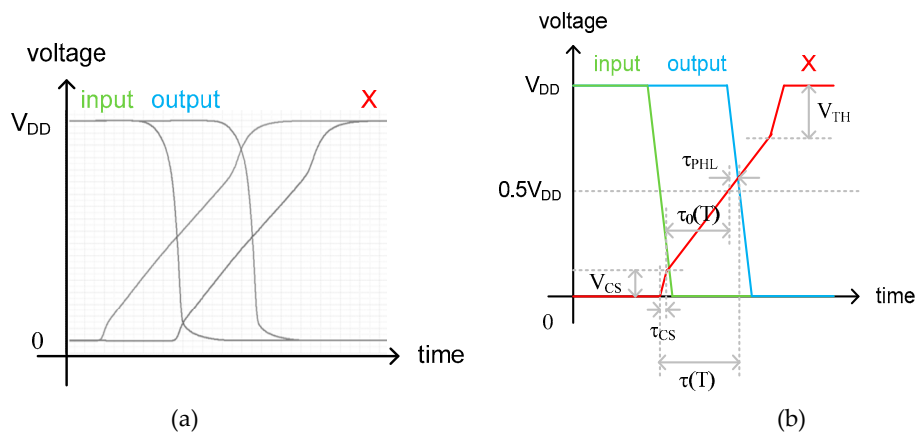


Figure 9. (a) Simulated and (b) theoretical waveforms of the fine delay cell.

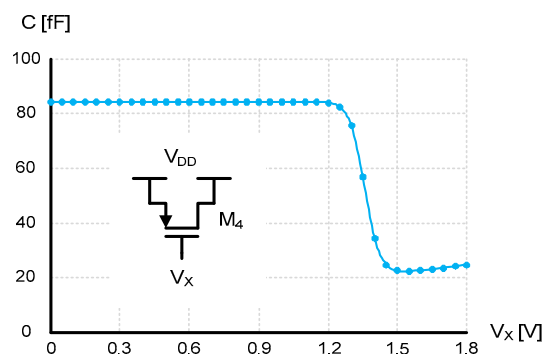


Figure 10. Capacitance versus voltage curve of the PMOS capacitor,  $M_4$ .

### 3.3. SAR Control Logic

In this temperature sensor, the SAR control logic updates the 9b data, DATA[8 : 0], periodically at the falling edge of CLK<sub>DELAYED</sub>. It sends DATA[8 : 0] to the 2<sup>9</sup> : 1 MUX to select the most appropriate one from 2<sup>9</sup> delayed clock signals until the delay time of the coarse and fine delay lines equals to 1/f<sub>REF</sub>.

Figure 11 shows the state diagram of the implemented SAR control logic. First, it starts from the 9b data, DATA[8 : 0], initialized as 100000000. This initial code points at the center of 2<sup>9</sup> fine delay cells of the fine delay line. When both rising edges of CLK and CLK<sub>DELAYED</sub> are compared by the DFF, as shown in Figure 4, it outputs 1 or 0 as a comparison result to the input of the SAR control logic. If the value is 1, it means that the rising edge of CLK is faster than the rising edge of CLK<sub>DELAYED</sub> and if the value is 0, vice versa. Depending on the input of the SAR control logic, DATA[8 : 0] is next updated to 110000000 or 010000000 and the 2<sup>9</sup>:1 MUX selects a faster or slower one from 2<sup>9</sup> delayed clock signals, as shown in Figure 11. After nine clock periods, i.e., 9/f<sub>REF</sub>, the SAR control logic finally outputs the 9b digital data as DATA[8 : 0].

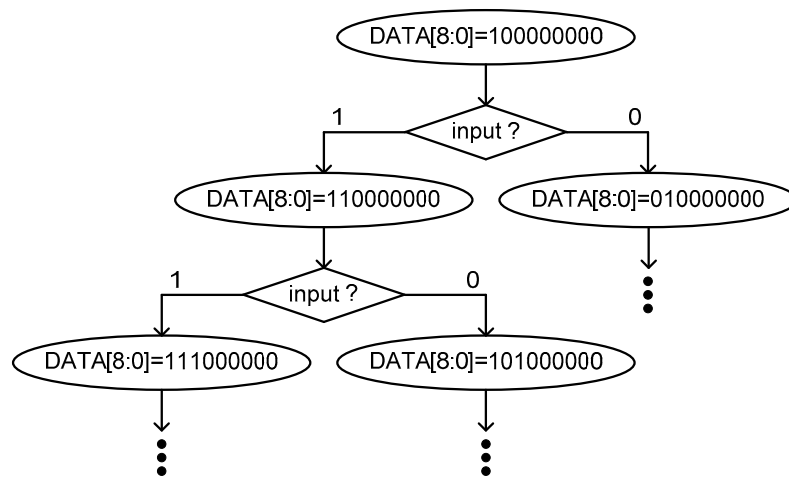


Figure 11. SAR state diagram.

Figure 12 shows the implemented SAR control logic. It consists of 20 DFFs and nine OR gates. Among the 20 DFFs, 11 DFFs on the upper side are used as the clock generator and nine DFFs on the lower side are used as the shift register to store the input value sequentially. Since an impulse clock signal like 010 is needed by only one of the nine DFFs at a time in the shift register, the leftmost DFF of the clock generator was designed as a different type of DFF which is reset to 1 rather than 0. All the other DFFs of the SAR control logic are reset to 0 when the START signal is low.

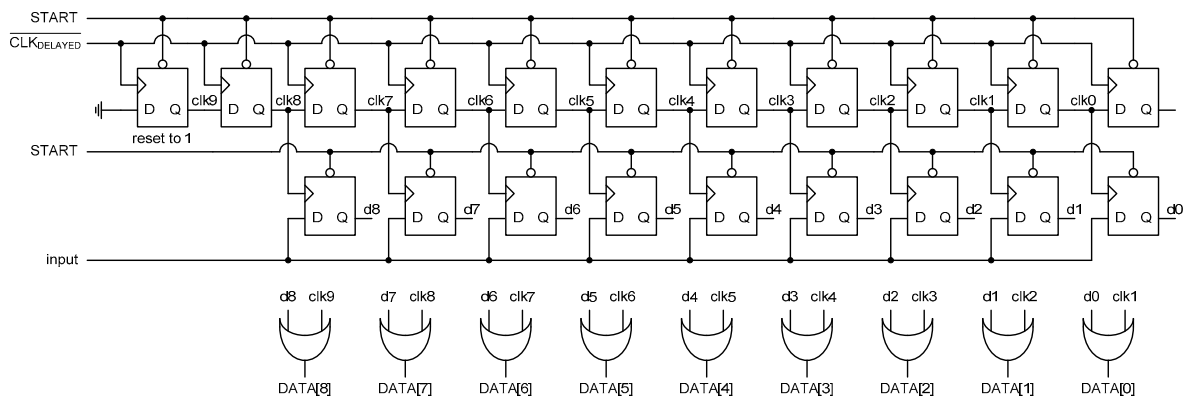


Figure 12. SAR control logic.

### 4. Measurements

The proposed temperature sensor was implemented in a standard 0.18  $\mu\text{m}$  1P6M bulk CMOS process with general  $V_{\text{TH}}$  transistors. Figure 13 shows the die photo and the FR4 PCB. The active die area was 0.432  $\text{mm}^2$ . It occupied a relatively large area because the fine delay line contained as many as  $2^9$  fine delay cells for a temperature resolution as low as 0.49  $^{\circ}\text{C}$  while covering up more than 0 to 100  $^{\circ}\text{C}$  of the temperature range with margins. Thus, the die area can be reduced if the temperature resolution and temperature range requirements are mitigated.

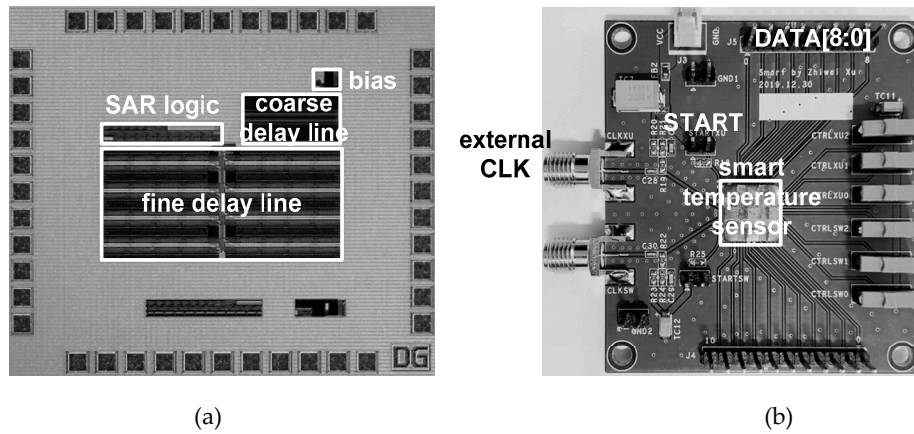


Figure 13. (a) Die photo and (b) FR4 PCB.

Figure 14 shows the measured temperature error over the range of 0 to 100  $^{\circ}\text{C}$  after one-point and two-point calibrations, respectively. The temperature error was measured with seven different temperature sensor chips in the temperature chamber, JEIO TC3-ME-025. For measurement accuracy, a PT100 RTD sensor (OMEGA PR-20 with DP32PT) was used as a reference. The measured temperature error varied from  $-6.1$  to  $+1.3$   $^{\circ}\text{C}$  after one-point calibration at 50  $^{\circ}\text{C}$  and from  $-1.6$  to  $+0.6$   $^{\circ}\text{C}$  after two-point calibration at 20 and 80  $^{\circ}\text{C}$ . Figure 15 shows the simulated temperature error after one-point and two-point calibrations, respectively. For the process corners, TT, FS, SF, FF and SS, the simulated temperature error varied from  $-15.0$  to  $+12.3$   $^{\circ}\text{C}$  after one-point calibration at 50  $^{\circ}\text{C}$  and from  $-1.6$  to  $+0.6$   $^{\circ}\text{C}$  after two-point calibration at 20 and 80  $^{\circ}\text{C}$ . This result agrees well with the derived Equation (6) in that  $X(T)$  is represented as  $aT + b$  and thus, we needed two-point calibration to compensate for the process variations in  $a$  and  $b$ .

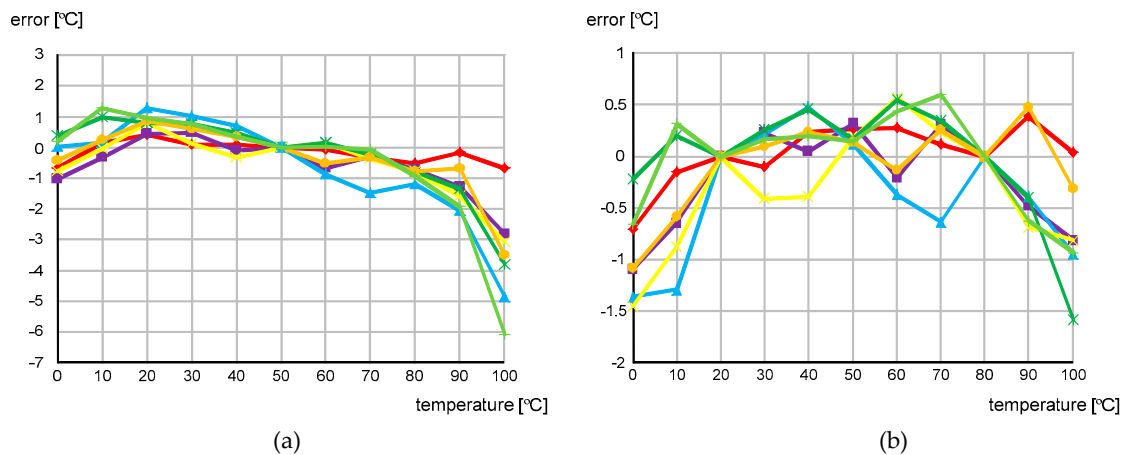
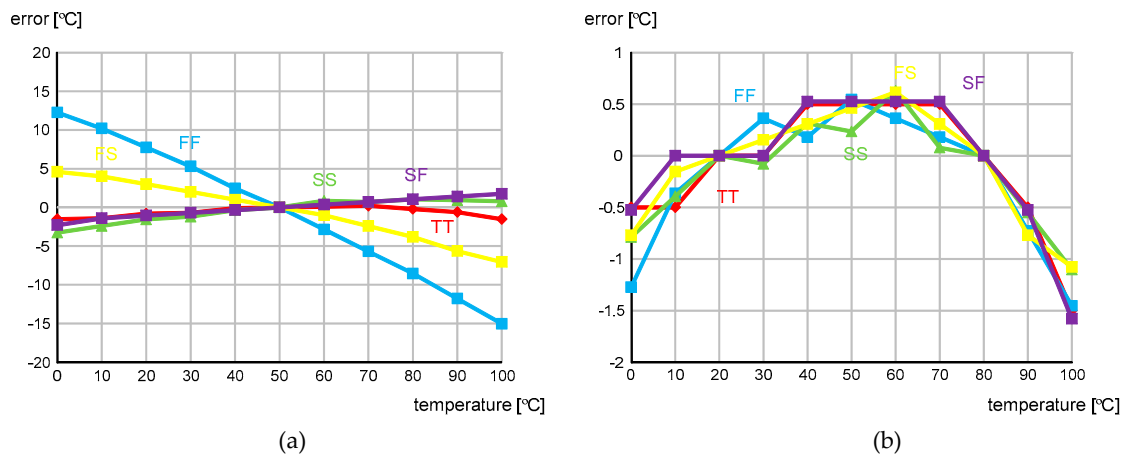
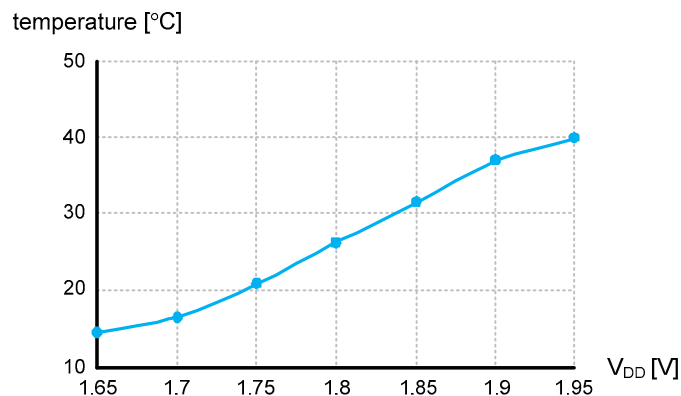


Figure 14. Measured temperature error after (a) one-point calibration and (b) two-point calibration.



**Figure 15.** Simulated temperature error after (a) one-point calibration and (b) two-point calibration for the process corners, TT, FS, SF, FF and SS.

The supply voltage sensitivity was measured as low as  $0.085\text{ }^{\circ}\text{C}/\text{mV}$  at  $27\text{ }^{\circ}\text{C}$  while  $V_{\text{DD}}$  varied from 1.65 to 1.95 V, as shown in Figure 16. From (6),  $X(T)$  is ideally independent of  $V_{\text{DD}}$  because it is not a function of  $V_{\text{DD}}$  at all. However, the  $X(T)$  of (6) was derived under the assumption that  $\tau_{\text{CS}}$  and  $\tau_{\text{PHL}}$  are much smaller than  $\tau_0(T)$ , and  $V_{\text{CS}}$  is also much smaller than  $V_{\text{DD}}$ , respectively. Since  $\tau_{\text{CS}}$ ,  $\tau_{\text{PHL}}$  and  $V_{\text{CS}}$  are very small but not zero,  $X(T)$  is slightly affected by  $V_{\text{DD}}$ . To reduce the supply voltage sensitivity, we canceled out  $V_{\text{DD}}$  in (5) by carefully designing  $I(T)$  to also be linear with  $V_{\text{DD}}$ , as shown in (2).



**Figure 16.** Measured  $V_{\text{DD}}$  sensitivity.

The reference clock frequency,  $f_{\text{REF}}$ , was 225 kHz. Since the temperature sensor operates based on the 9b SAR control logic, the conversion rate was 25 kHz and the energy efficiency was  $7.2\text{ nJ}/\text{sample}$ . Figure 17 shows the power consumption breakdown at  $25\text{ }^{\circ}\text{C}$ . Sixty-three percent of the total power was consumed by the temperature-dependent current bias circuit and 32% was consumed by the coarse and fine delay lines. Table 1 compares the implemented temperature sensor with the previous time domain CMOS temperature sensors implemented in  $0.13\text{ }\mu\text{m}$  or  $0.18\text{ }\mu\text{m}$  CMOS technologies. Compared to previous works, this temperature sensor had a relatively fast conversion rate.

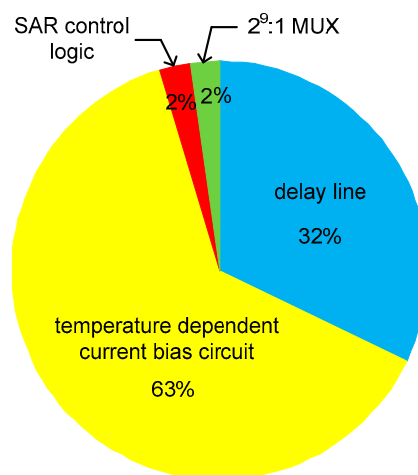


Figure 17. Power consumption breakdown.

Table 1. Performance summary.

	[11]	[14]	[16]	[20]	[21]	This Work
CMOS technology	0.13 $\mu\text{m}$	0.18 $\mu\text{m}$	0.18 $\mu\text{m}$	0.18 $\mu\text{m}$	0.18 $\mu\text{m}$	0.18 $\mu\text{m}$
Die area	0.12 $\text{mm}^2$	0.0324 $\text{mm}^2$	0.09 $\text{mm}^2$	0.074 $\text{mm}^2$	0.19 $\text{mm}^2$	0.432 $\text{mm}^2$
Supply voltage	1.2 V	1.0 V	1.2 V	0.8 V	1.2 V	1.8 V
Temperature range	0~100 $^{\circ}\text{C}$	0~100 $^{\circ}\text{C}$	0~100 $^{\circ}\text{C}$	−20~80 $^{\circ}\text{C}$	−40~85 $^{\circ}\text{C}$	0~100 $^{\circ}\text{C}$
Resolution	0.78 $^{\circ}\text{C}$	0.3 $^{\circ}\text{C}$	0.3 $^{\circ}\text{C}$	0.145 $^{\circ}\text{C}$	0.18 $^{\circ}\text{C}$	0.49 $^{\circ}\text{C}$
Accuracy	−4.0~4.0 $^{\circ}\text{C}$	−0.8~1.0 $^{\circ}\text{C}$	−1.4~1.5 $^{\circ}\text{C}$	−0.9~1.2 $^{\circ}\text{C}$	−1.0~1.0 $^{\circ}\text{C}$	−1.6~0.6 $^{\circ}\text{C}$
Conversion rate	5 kHz	1 kHz	33.3 Hz	1.2 Hz	1kHz	25 kHz
Energy	0.24 $\mu\text{J}/\text{sample}$	0.41 $\text{nJ}/\text{sample}$	2.2 $\text{nJ}/\text{sample}$	8.9 $\text{nJ}/\text{sample}$	–	7.2 $\text{nJ}/\text{sample}$
$V_{\text{DD}}$ sensitivity	1.6 $^{\circ}\text{C}/\text{mV}$	–	0.014 $^{\circ}\text{C}/\text{mV}$	0.0038 $^{\circ}\text{C}/\text{mV}$	–	0.085 $^{\circ}\text{C}/\text{mV}$

## 5. Conclusions

In this paper, we defined the temperature estimation function,  $X(T)$ , and categorized the time domain CMOS temperature sensors into 12 types. By choosing  $X(T) = 1/f_{\text{REF}}/\tau(T)$ , we implemented a new type of time domain CMOS temperature sensor with a 9b SAR control logic and a fine delay line. Although the chip has a relatively large die area, it can achieve a comparable temperature resolution and linearity error. The supply voltage sensitivity could be fairly reduced by carefully designing  $I(T)$  to cancel out  $V_{\text{DD}}$  in  $\tau(T)$ .

**Author Contributions:** Conceptualization, S.B.; methodology, Z.X.; validation, Z.X. and S.B.; investigation, Z.X.; writing-original draft preparation, Z.X.; writing-review and editing, S.B.; supervision, S.B.; funding acquisition, S.B. All authors have read and agreed to the published version of the manuscript.

**Funding:** This research was supported by Basic Science Research Program through the National Research Foundation of Korea (NRF) funded by the Ministry of Education (NRF-2017R1D1A1B03028325).

**Acknowledgments:** The authors would like to thank IC Design Education Center (IDEC), Daejeon, South Korea, for supporting MPW and EDA tools.

**Conflicts of Interest:** The authors declare no conflict of interest.

## References

1. Yousefzadeh, B.; Heidary, S.; Makinwa, A.A. A BJT-based temperature-to-digital converter with  $\pm 60$  mK ( $3\sigma$ ) inaccuracy from  $-55$   $^{\circ}\text{C}$  to  $+125$   $^{\circ}\text{C}$  in 0.16- $\mu\text{m}$  CMOS. *IEEE J. Solid-State Circuits* **2017**, *52*, 1044–1052. [\[CrossRef\]](#)
2. Oshita, T.; Shor, J.; Duarte, D.E.; Kornfeld, A.; Zilberman, D. Compact BJT-Based Thermal Sensor for Processor Applications in a 14 nm tri-Gate CMOS Process. *IEEE J. Solid-State Circuits* **2015**, *50*, 799–807. [\[CrossRef\]](#)
3. Tang, Z.; Tan, N.N.; Shi, Z.; Yu, X.-P. A 1.2V Self-Referenced Temperature Sensor with a Time-Domain Readout and a Two-Step Improvement on Output Dynamic Range. *IEEE Sens. J.* **2018**, *18*, 1849–1858. [\[CrossRef\]](#)

4. Shor, J.S.; Luria, K. Miniaturized BJT-Based Thermal Sensor for Microprocessors in 32- and 22-nm Technologies. *IEEE J. Solid-State Circuits* **2013**, *48*, 2860–2867. [[CrossRef](#)]
5. Park, H.; Kim, J. A 0.8-V Resistor-Based Temperature Sensor in 65-nm CMOS With Supply Sensitivity of 0.28 °C/V. *IEEE J. Solid-State Circuits* **2018**, *53*, 906–912. [[CrossRef](#)]
6. Pan, S.; Luo, Y.; Shalmany, S.H.; Makinwa, K.A.A. A Resistor-Based Temperature Sensor With a 0.13 pJ K2 Resolution FoM. *IEEE J. Solid-State Circuits* **2018**, *53*, 164–173. [[CrossRef](#)]
7. Deng, F.; He, Y.; Li, B.; Zhang, L.; Wu, X.; Fu, Z.; Zuo, L. Design of an Embedded CMOS Temperature Sensor for Passive RFID Tag Chips. *Sensors* **2015**, *15*, 11442–11453. [[CrossRef](#)]
8. Sonmez, U.; Sebastiano, F.; Makinwa, K.A.A. Compact Thermal-Diffusivity-Based Temperature Sensors in 40-nm CMOS for SoC Thermal Monitoring. *IEEE J. Solid-State Circuits* **2017**, *52*, 1–10.
9. Ituero, P.; López-Vallejo, M.; Lopez-Barrio, C. A 0.0016 mm<sup>2</sup> 0.64 nJ Leakage-Based CMOS Temperature Sensor. *Sensors* **2013**, *13*, 12648–12662. [[CrossRef](#)]
10. Xie, S.; Theuwissen, A.J.P. On-Chip Smart Temperature Sensors for Dark Current Compensation in CMOS Image Sensors. *IEEE Sens. J.* **2019**, *19*, 7849–7860. [[CrossRef](#)]
11. Ha, D.; Woo, K.; Meninger, S.; Xanthopoulos, T.; Crain, E.; Ham, N. Time-Domain CMOS Temperature Sensors With Dual Delay-Locked Loops for Microprocessor Thermal Monitoring. *IEEE Trans. Very Large Scale Integr. (VLSI) Syst.* **2011**, *20*, 1590–1601. [[CrossRef](#)]
12. Chen, P.; Chen, C.-C.; Tsai, C.-C.; Lu, W.-F. A time-to-digital-converter-based CMOS smart temperature sensor. *IEEE J. Solid-State Circuits* **2005**, *40*, 1642–1648. [[CrossRef](#)]
13. Chen, P.; Chen, C.-C.; Peng, Y.-H.; Wang, K.-M.; Wang, Y.-S. A time-domain SAR smart temperature sensor with curvature compensation and a 3 $\sigma$  inaccuracy of  $-0.4$  °C ~  $+0.6$  °C over a 0 °C to 90 °C range. *IEEE J. Solid-State Circuits* **2010**, *45*, 600–609. [[CrossRef](#)]
14. Law, M.-K.; Bermak, A. A 405-nW CMOS Temperature Sensor Based on Linear MOS Operation. *IEEE Trans. Circuits Syst. II Express Briefs* **2009**, *56*, 891–895. [[CrossRef](#)]
15. Lin, Y.-S.; Sylvester, D.; Blaauw, D. An ultra low power 1V, 220nW temperature sensor for passive wireless applications. In Proceedings of the 2008 IEEE Custom Integrated Circuits Conference, San Jose, CA, USA, 21–24 September 2008; pp. 507–510.
16. Jeong, S.; Foo, Z.; Lee, Y.; Sim, J.-Y.; Blaauw, D.; Sylvester, D. A Fully-Integrated 71 nW CMOS Temperature Sensor for Low Power Wireless Sensor Nodes. *IEEE J. Solid-State Circuits* **2014**, *49*, 1682–1693. [[CrossRef](#)]
17. Vaz, A.; Ubarretxena, A.; Zalbide, I.; Pardo, D.; Solar, H.; Garcia-Alonso, A.; Berenguer, R. Full Passive UHF Tag With a Temperature Sensor Suitable for Human Body Temperature Monitoring. *IEEE Trans. Circuits Syst. II Express Briefs* **2010**, *57*, 95–99. [[CrossRef](#)]
18. Hwang, S.; Koo, J.; Kim, K.; Lee, H.; Kim, C. A 0.008mm<sup>2</sup> 500 $\mu$ W 469kS/s frequency-to-digital converter based CMOS temperature sensor with process variation compensation. *IEEE Trans. Circuits Syst.* **2013**, *60*, 2241–2248. [[CrossRef](#)]
19. Anand, T.; Makinwa, K.A.A.; Hanumolu, P.K. A VCO Based Highly Digital Temperature Sensor With 0.034 °C/mV Supply Sensitivity. *IEEE J. Solid-State Circuits* **2016**, *51*, 2651–2663. [[CrossRef](#)]
20. Someya, T.; Islam, A.M.; Sakurai, T.; Takamiya, M. An 11-nW CMOS Temperature-to-Digital Converter Utilizing Sub-Threshold Current at Sub-Thermal Drain Voltage. *IEEE J. Solid-State Circuits* **2019**, *54*, 613–622. [[CrossRef](#)]
21. Tran, T.-H.; Peng, H.-W.; Chao, P.C.-P.; Hsieh, J.-W. A log-ppm digitally controlled crystal oscillator compensated by a new 0.19-mm<sup>2</sup> time-domain temperature sensor. *IEEE Sens. J.* **2017**, *17*, 51–62. [[CrossRef](#)]
22. Tang, Z.; Fang, Y.; Shi, Z.; Yu, X.-P.; Tan, N.N.; Pan, W. A 1770- $\mu$ m<sup>2</sup> Leakage-Based Digital Temperature Sensor with Supply Sensitivity Suppression in 55-nm CMOS. *IEEE J. Solid-State Circuits* **2020**, *55*, 781–793. [[CrossRef](#)]

